

Atom beam triangulation of organic layers at 100 meV normal energy: self-assembled perylene on Ag(110) at room temperature

Nataliya Kalashnyk¹ and Philippe Roncin^{1,*}

¹*Institut des sciences moléculaires d'Orsay (ISMO), CNRS,
Univ. Paris-Sud, Université Paris-Saclay, Orsay F-91405, France*

The controlled growth of organic layer on surface is still awaiting for an on-line reliable monitoring that would allow improvement of its quality. We show here that the self-assembly of the perylene monolayer deposited on Ag(110) at room temperature can be tracked with low energy atoms in a regime where the energy perpendicular to the layer is less than 0.1 eV preventing damage to the layer. The image processing required for this triangulation technique with atoms is described in details.

I. INTRODUCTION

Thin films of polycyclic aromatic hydrocarbon such as perylene ($C_{20}H_{12}$) are rigorously investigated for their broad applications, for instance in OLED. A large number of studies over the last decade have evidenced crucial effects of molecular organization on such films properties. This assembly can be investigated locally in great details by STM [1] and or AFM but not during growth. This limitation does not exist with reflection high energy electron diffraction widely used in molecular beam epitaxy. However, it is too destructive for such fragile layer so that there is a clear lack of technique to monitor on-line the nature of the molecular arrangement and its quality. Using the same grazing incidence geometry compatible with on-line operation, two techniques sensitive only to the topmost layer have recently been developed; fast atom diffraction (GIFAD or FAD) [3, 4] and fast ion or atom beam triangulation (IBT) [4–8]. These techniques developed for mineral crystals operate at comparatively high projectile energy. A new regime of extremely weak interaction with the surface is briefly presented, and applied to the investigation perylene assembly on Ag(110). A simple image processing providing a more efficient triangulation technique is described in details. The convergence between GIFAD and IBT is discussed at the end.

A. IBT and GIFAD

IBT is a technique to identify the low index direction of the topmost layer. It is based on the fact that a beam shed at a surface under grazing angle of incidence will experience very different physical condition if it is aligned or not with a low index direction. Several physical properties have been exploited depending on the nature and energy E_0 of the projectile. For protons with $E_0=25$ keV at incidence angle $\theta_{in}=1.6$ deg. with respect to the Cu(001) surface (i.e. a normal energy $E_{\perp} = E_0 \sin(\theta_{in})^2 \approx 20$ eV), monitoring of the electric current flowing to the target

during the azimuthal scan turned out [6] to be a simple technique. This is an indirect measure of the emission of secondary electrons and the contrast appears because projectiles undergoing multiple bounces [9] along so called surface channeling have more chance to trigger electron emission than those which do not. This interpretation was confirmed using an electron detector, which also provides higher sensitivity [8] allowing a reduced beam intensity. At such comparatively high projectile normal energy, the initial projectile charge state has little consequences and similar contrast was observed with neutral hydrogen projectiles [7]. Only recently the same triangulation strategy was applied with lower energy atoms having only 2 keV energy and a perpendicular energy E_{\perp} between 0.6 and 1 eV [4, 5]. In this case there is no electron emission and the azimuthal scan is performed by monitoring the variation of the peak intensity of the scattering profile. The azimuthal contrast is generated by the fact that along the channeling directions the successive momentum transfers add up instead of being randomly distributed otherwise. As a result the scattered beam is broader having a lower peak intensity generating dips at each low index direction. We explore here the same principle at even lower normal energies, with 300 eV helium atoms having E_{\perp} in the 50-100 meV range. This energy range was chosen because it corresponds to the conditions where diffraction has been observed giving birth to the GIFAD technique. If the transverse coherence Δ_x of the atomic beam is larger than the lattice parameter d , diffraction can be observed as Bragg peaks separated by a reciprocal lattice vector $G = 2\pi/d$ in the scattering profile. The transverse coherence is here a simple statistical property of the beam expressed as $\Delta_x = 2\pi/\Delta_k$ with $\Delta_k = k_0\Delta\psi$, where k_0 is the momentum of the atoms and $\Delta\psi$ is the angular divergence of the beam. The additional information provided by the lattice parameter is already extremely valuable to complement the triangulation. Indeed triangulation provides the directions of alignment but does not specify the size of the unit cell nor the number of molecules in this cell whereas even faint diffraction does provide this absolute dimension of the unit cell. In addition, when nice elastic diffraction spots are observed, then the profile of the surface electronic density can be retrieved with excep-

*Electronic address: philippe.roncin@u-psud.fr

tional accuracy [10, 11]. However, it should be noted that this high resolution regime has not been achieved so far for molecular layers. Clear diffraction lines have been recently reported [4, 5] for comparatively small, non planar alanine molecules chemically adsorbed on a Cu(110) surface. The present paper reports experimental investigation of the perylene self-assembly on Ag(110), a planar molecule which show significantly lower interaction with the surface leading to partial flexibility in such organic monolayer. Only weak diffraction is observed probably due to metastability of the layer pushing us to develop a new simple and robust procedure for triangulation with low energy atoms.

II. EXPERIMENTAL SETUP

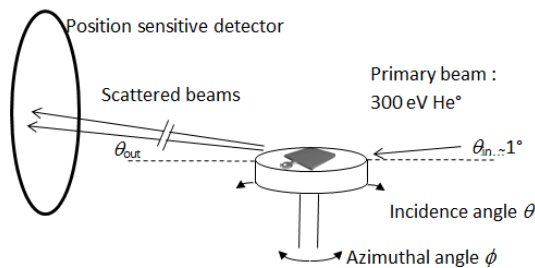


FIG. 1: Scheme of the experimental setup. The surface is placed on a Omicron plate depicted in gray in the center and exposed to the 300 eV He⁺ beam at grazing incidence. The scattered beams are detected almost a meter downstream on a position sensitive detector imaging the outgoing angles.

The deposition of perylene monolayer on Ag(110) surface were conducted in an UHV system equipped with standard facilities for sample preparation and analysis as well as a separate load-lock chamber compatible with a high performance portable UHV suitcase. The Ag(110) surface was cleaned by several cycles of ion sputtering followed by annealing. The perylene molecules were evaporated on Ag(110) held at room temperature and the assembly were subsequently checked with MCP-LEED system operated at 18 eV electron energy to increase surface sensitivity and avoid damage of organic layer. The sample was then transferred by means of the portable UHV suitcase into the independent GIFAD chamber without breaking the UHV conditions. The surface is mounted perpendicular to the rotation axis of a standard X,Y,Z, ϕ sample manipulator itself mounted on a custom designed tilt system controlling the angle of incidence θ (see fig.1). The atomic beam of 300 eV neutral helium passes into the vacuum chamber through a 100 μ m circular hole. Before inserting the sample, the beam position is recorded onto the position sensitive detector made of microchannel-plates in front of a phosphor screen and filmed by a CCD camera. Then the surface is progressively inserted in the beam and the angle of incidence is tuned to 0.7 degree.

Most often, the surface is only partially inserted into the beam leaving a small part of the beam flying over the surface without interaction producing a small reference spot on the detector as can be seen in the bottom of scattering patterns in fig.2.

III. RESULTS

An encouraging diffraction signal was observed on the same day when the sample was introduced but could not be found again the day after with exactly the same conditions. Therefore a systematic azimuthal scan was decided. In principle, the only thing needed for such a scan is to program a continuous or stepwise rotation synchronized with a movie or with a sequence of images. This has not been possible because the surface plane (defined by its normal vector) was found to be misaligned with the rotation axis by approximately 1 deg., see azimuthal scans in fig.6 below. An automatic compensation could have been programmed (as detailed in [12]). In the present case, approximate manual corrections of the angle of incidence θ were needed every few images to maintain the scattering profile in the same region on the detector. Each image of the scattering profile is made of a fifty exposure of 2 s directly added inside the CCD camera before transfer to the PC. The consequence is that to perform the azimuthal scan in reasonable time, a comparatively large angular ϕ steps of two degrees were chosen. At such long exposure, the camera has a significant noise and a dark image was also recorded with exactly the same exposure conditions but with the beam valve closed. This dark image is automatically subtracted from all images.

A. Data analysis

Six successive images of a region of interest in the the detector are displayed in figure 2. At first glance these images look rather similar with a smooth scattering profile without any evidence of Bragg peaks. A closer inspection reveals that the pattern undergoes profound variations. The white quasi-elliptic contour line undergoes an anti-clockwise rotation between images 2a) and 2c) whereas the evolution between images 2d) and 2f) is clockwise. Between 2c) and 2d) the variation is more drastic with a sudden mirror change of the orientation. This behavior is characteristic of surface channeling of ions or atoms along a low index direction. Since the energy is more than 100 times less than in [6, 8] we try to clarify the specific dynamics occurring as the projectiles direction approaches a low index direction at various energies. At high normal energy $E_{\perp} \gtrsim 10$ eV the projectiles penetrate deeply the surface electronic density. The curves of iso-electronic density are no longer a 2D surface over the surface atoms but become separated spheroids centered around the atoms so that some projectile trajectory

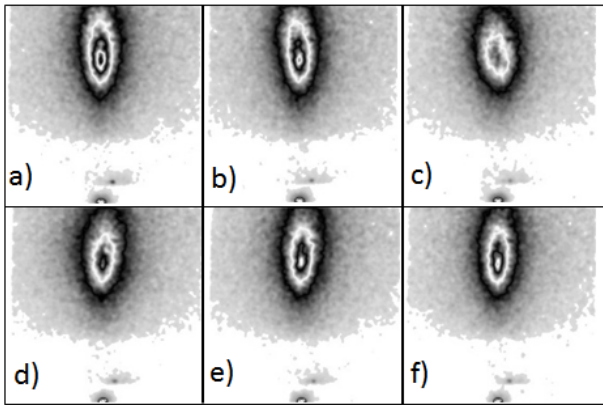


FIG. 2: Raw images of the scattering pattern recorded every two deg. azimuth. The relative orientation is as sketched in fig.1 i.e. the surface plane is horizontal while the outgoing scattering angle θ_{out} increases along the vertical direction. The color scale is a fixed black and white banded palette highlighting a quasi-elliptic white contour. Label a) to f) are reported on fig.5.

may even penetrate below the surface. However, most of the trajectories simply bounce in between the rows of surface atoms [13] and undergo multiple collisions from one side of the channel to the other allowing a genuine guiding and specific rainbows [24]. At $E_{\perp} \lesssim 100\text{meV}$ used in this work, the evolution when the beam direction approaches a low index direction has been measured in details in the diffraction regime [14, 15] and is well described by quantum mechanics [16] or semi-classical models for weak surface corrugation [17]. In this regime the net deflection of the beam is very limited and is localized at scattering angles significantly larger than the specular angle [14–16]. In the present case the later effect is likely to be responsible for the clear rotation of the top of the contour ellipses in fig.2. As noted in [15] this mean twist angle of the ellipse is a differential signal which points to zero twist angle when the beam is perfectly aligned as well as in random directions. To identify these directions, we concentrate on robust features of the scattering pattern such as the horizontal or vertical intensity profiles. The associated widths of the observed distribution seem an obvious choice but we have to take into account that, due to the tilt angle with the manipulator axis, the angle of incidence θ_{in} could not be kept constant. We have decided to transform our 2D images in a coordinate system which is less sensitive to variation of the angle of incidence.

1. Polar coordinates

The Cartesian coordinates on the raw images in fig.2 correspond to scattering angles parallel and perpendicular to the surface. For scattering problems in general, the magnitude of the deflection and the associated polar profile

are more relevant. This is for instance the case of scattering rainbows observed at grazing incidence which are known since decades to occur at fixed polar angle α (see fig.3) over a wide range of incidence angle. This is also the case for supernumerary rainbows [18]. This is still valid in the quantum scattering regime where diffraction charts show clear nodal structure well-aligned along polar angle. In fact these nodal structures transform into attenuating supernumerary rainbows when diffraction is not visible anymore. The use of these coordinates should provide image properties hardly sensitive to the actual angle of incidence.

2. Polar-like 2D transformation

A pragmatic choice is to consider the position of the direct beam as a reference in the raw image as well as for the transform. Taking $(0,0)$ for the beam coordinates, each pixel of coordinates (k_x, k_y) is part of a circle having a center (k_{xc}, k_{yc}) given by $k_{xc} = 0$ and $k_{yc} = k_y/2 + k_x^2/k_y$ and a radius $k_{eff} = k_{yc}$ and $\alpha = \sin^{-1}(k_x/k_{eff})$. This polar-like transform $(k_x, k_y) \rightarrow (\alpha, 2k_{eff})$ is defined everywhere above the direct beam ($k_y > 0$). Also to provide a metric close to the original one, the polar angles are reported between -90 deg. and $+90$ deg. only, corresponding to the upper parts of the circles in fig.3. Note that it does not affect at all the vertical line above the direct beam i.e. the scattering profile in the incidence plane. It does not seriously affect the general shape of the scattering patterns, see fig.3a) and fig.3b).

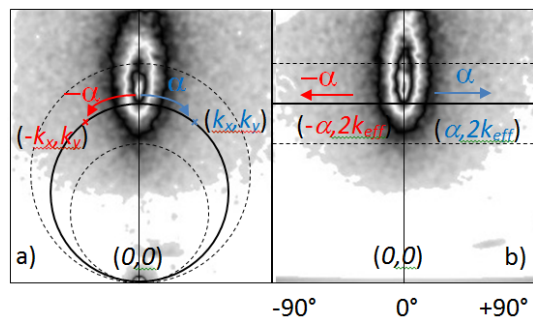


FIG. 3: Sketch of the polar-like transform associating a coordinate (k_x, k_y) fig.a) to new coordinates $(\alpha, 2k_{eff})$ fig.b) defined as follow. k_{eff} is the radius of the circle the point (k_x, k_y) , its left/right symmetric $(-k_x, k_y)$ as well as the direct beam. This forces the center to lie on vertical axis above the primary beam i.e. in the plane of incidence. Finally, α is the polar angle along this circle. In this transformation, the incidence plane (vertical line) is strictly invariant and most of the image is hardly affected.

3. 1D scattering and polar profiles

The scattering profile in the plane of incidence is comparatively broad and it is reasonably well fitted by a log-normal distribution rather common in atom surface scattering [19, 20]. This profile is used here only to measure the location of the maximum. All polar plots $P(\alpha)$ used for the azimuthal scan correspond to a slice of -0.2 deg. below the maximum of this scattering distribution. Two examples of polar angle distribution are displayed in fig.4 and empirically fitted by a Lorentzian profile to extract the three parameters; the mean value $\langle\alpha\rangle$, the width W_α and the intensity.

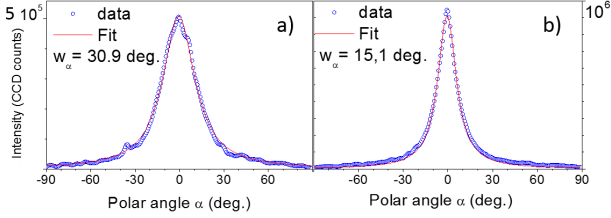


FIG. 4: Polar scattering profiles $P(\alpha)$. The one on the left a) corresponds to the images displayed in fig.2c) while the one on the right b) is derived from fig.2f) also in fig.3a).

B. Azimuthal scans

The fig. 5 displays a nice azimuthal scan of the measured Lorentzian width W_α evidencing the presence of low index directions. Note that, instead of polar coordinate, almost the same result could be obtained by dividing the horizontal width by the mean scattering angle directly from raw images without polar transform. The more rigorous, polar approach was adopted here with a nice counterpart that the tilt angle can be measured directly. The fig. 6 shows a smooth evolution of the mean polar angle $\langle\alpha\rangle_{bottom}$ as measured by the fit on the bottom part of the scattering distribution defined as 0.2 deg. below the maximum pointed by the log-normal fit of the vertical profile. This smooth evolution is adjusted with a pure sine function with a full amplitude of 4 deg. This corresponds to a tilt angle of $\tau = 1$ deg. as sketched in fig.7. It should be mentioned that in the natural angular frame of the detector (referred to as the Cartesian frame above) this angular swing is only 0.05 deg. since the typical value of θ_{eff} representing the radius of the circle in fig.3 corresponds to 0.7 deg. As a naive attempt to capture the rotation of the ellipse visible in fig.2 we have also measured the mean polar angle $\langle\alpha\rangle_{top}$ of a 0.2 deg. wide slice on top of all images and subtracted it from the one $\langle\alpha\rangle_{bottom}$ defined above and which is measured in the 0.2 degree slice below the maximum. The figure 6 shows bipolar oscillation around the low index directions identified in fig.5. This nicely illustrates the rotation effect of the quasi-ellipse.

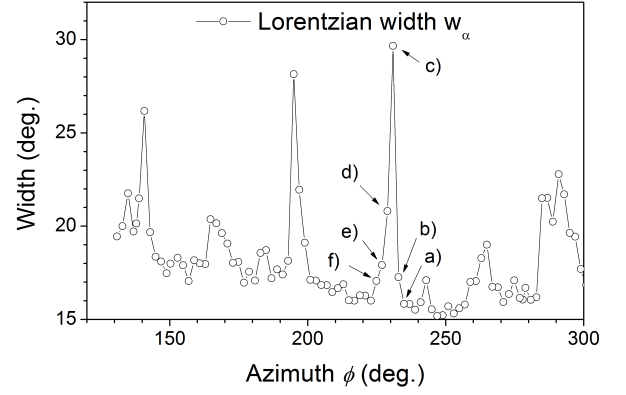


FIG. 5: Azimuthal scan of the polar width as measured by a Lorentzian fit (see e.g. fig.4). The scan outlines sharp variation taking place within one or two degrees. The six labels a) to f) are the same as used in fig.2.

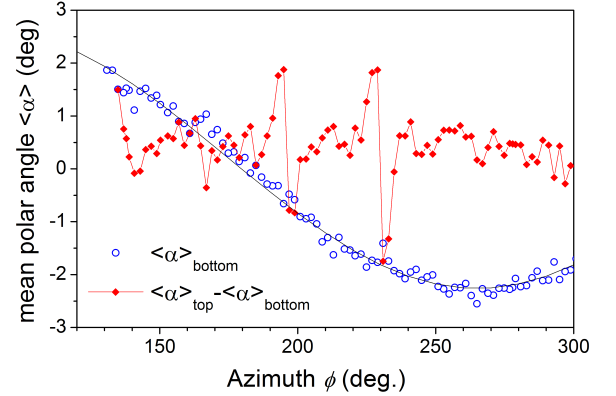


FIG. 6: Azimuthal scan of the center $\langle\alpha\rangle_{bottom}$ of the polar profile (\circ) as measured by the Lorentzian fit in fig.5 in the bottom part of the images. The diamonds (\diamond) plot the difference with the same quantity $\langle\alpha\rangle_{top}$ measured in the upper part of the same scattering images.

Combining the azimuthal scan in fig.5 together with the initial GIFAD diffraction and LEED data is comparatively easy because all pieces of information are very complementary, however, this will not be discussed here. The reason is that we lack the redundancy of a complete azimuthal scan and, more important, the rapid degradation of the sample in a single day at pressure below 10^{-10} mbar demonstrates that the molecular organization is metastable preventing complete confidence that diffraction and triangulation measurement were actually observing the same structure. This doubt was also triggered by the fact that our observation does not directly match the direct STM imaging after a comparable preparation. This is probably due to the fact that the system seems very sensitive to the density of deposited molecules

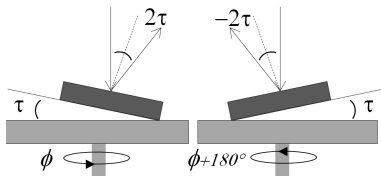


FIG. 7: sketch of the maximum effect of a tilt angle τ between the surface (dark gray) and the rotation axis (light grey) on the specular reflection in the polar coordinates

so that there could be gradual transition from densely packed comparatively well-organized layer to looser organization [1].

IV. DISCUSSION

The present experimental condition were chosen to track diffraction features. This has led to tedious recording of more than 100 successive images each exposed during 100 seconds with additional manual control stretching overall almost ten hours. One of the reasons was that the scattering on the surface showed comparatively low reflectivity, the other being due to the corrections imposed by the tilt angle. However, even without any tilt of the surface i.e. without any need for manual control this would have required three hours of beam time. This can be drastically reduced by noting that the smaller structure observed in the images is on the order of 0.08 degree fwhm so that, if triangulation only had been targeted, the two $100\mu\text{m}$ diaphragms reducing the beam divergence below 0.02 deg. could have been replaced by two $400\mu\text{m}$ diaphragms allowing 256 times larger intensity. A scan would take less than 10 min without any loss. Indeed resolution scales with the diameters of the diaphragms but the beam intensity scales with the fourth power of the diameters. Another order of magnitude bringing acquisition time close to a minute is probably possible if one compromises further the resolution or using a more sophisticated image processing algorithm. Scanning time shorter than a minute are probably not relevant since fast mechanical action under vacuum is usually not recommended. This is still compatible with on-line analysis given the associate benefit that molecular growth is usually more uniform on a rotating sample. Finally, the comparatively low angular resolution of the present study can be improved by a continuous recording while image statistics can be recovered by running average between successive images.

The width technique detailed here is similar in essence to the one reported in [5] where the peak intensity of the scattering profile is used. Both approaches can probably be further improved and generalized by a generic multipolar expansion of the recorded images to extract the main scattering parameters, mean values, width, peak intensity and more sophisticated one as the k_x, k_y corre-

lation terms quantifying the orientation of the scattering pattern. The other aspect illustrated here is that triangulation is less demanding than diffraction. This can be extremely useful to extend the range of operation of GIFAD. Such a tolerance to local disorder can be understood in terms of the surface coherence length L_S defined as the mean distance without defect. This distance should be compared with the mean length L_T of the atom trajectory on the surface as can be estimated from classical trajectories or simple models [21]. Elastic diffraction can only occur if $L_S \gg L_T$ and has not been observed so far for any molecular layers. If $L_S \gtrsim L_T$ inelastic diffraction can be observed providing accurate lattice parameter but more difficult to interpret quantitatively in terms of surface electronic density. If $L_S \lesssim L_T$ then no diffraction should be observable, however the momentum transferred to the projectile atom along its trajectory is still very much influenced by local molecular alignment as probed in triangulation. In other words triangulation is likely to identify the local order over a much broader range of surface coherence length (i.e. global order). Meanwhile inelastic diffraction and possibly elastic diffraction will progressively show up only as the layer quality improves. Both IBT and GIFAD have demonstrated to be only sensitive to the topmost layer and have shown to be able to count the exact number of successive layers [22, 23] during growth. Both approaches are fully compatible and obviously needed to help monitoring on-line the growth of very good molecular layers. The very encouraging new aspect demonstrated here is that azimuthal scans are well-contrasted even with the low energies needed for GIFAD so that the $E_{\perp} \lesssim 1\text{eV}$ used here should not induce any damage to the fragile organic layer.

V. CONCLUSION

At first sight, it seems rather illusory to record an azimuthal dependence at one degree of incidence, of a surface itself tilted by more than a degree! Without any active correction this is clearly impossible. With manual pseudo random action this becomes possible but this induces such large intensity variation that only a shape analysis of the images, as detailed here, can partially restore significant variations. We have demonstrated that this turn out to be rather simple and that doing triangulation with a position sensitive detector is certainly a good choice. Triangulation becomes compatible with GIFAD offering much less strict constraints on the level of organization so that the growth of molecular layer can be monitored over a very broad range of relative disorder.

VI. ACKNOWLEDMENT

We are grateful to H. Khemliche, A. Momeni and L. Guillemot for their assistance in running the GIFAD setup and the transfer chamber.

-
- [1] K. Bobrov, N. Kalashnyk, and L. Guillemot, *The Journal of Chemical Physics* **142**, 101929 (2015)
 - [2] G. Witte, K. Hänel, S. Söhnchen, C. Wöll, *Appl. Phys. A* **82**, 447455 (2006)
 - [3] A. Zugarramurdi, M. Debiossac, P. Lunca-Popa, A. J. Mayne, A. Momeni, A. G. Borisov, Z. Mu, P. Roncin and H. Khemliche, *Appl. Phys. Lett.* **106**, 101902 (2015)
 - [4] J. Seifert, M. Busch, E. Meyer, and H. Winter, *Phys. Rev. Lett.* **111**, 137601 (2013).
 - [5] J. Seifert, M. Busch, E. Meyer, and H. Winter, *Phys. Rev. B* **89**, 075404 (2014).
 - [6] R. Pfandzelter, T. Bernhard, and H. Winter *Phys. Rev. Lett.* **90**, 036102 (2003).
 - [7] J. Seifert, E. Meyer, H. Winter, H. Kuhlenbeck - *Surface science*, **606**, L41L44 (2012)
 - [8] T. Bernhard, M. Baron, M. Gruyters, and H. Winter, *Phys. Rev. Lett.* **95**, 087601 (2005)
 - [9] A. Redinger, H. Hansen, U Linke, Y Rosandi, HM Urbassek, T Michely, *Phys. Rev. Lett.* **96**, 106103 (2006)
 - [10] M. Debiossac, A. Zugarramurdi, H. Khemliche, P. Roncin, A. G. Borisov, A. Momeni, P. Atkinson, M. Eddrief, F. Finocchi, and V. H. Etgens, *Phys. Rev. B* **90**, 155308 (2014).
 - [11] A. Schüller, S. Wethekam, D. Blauth, H. Winter, F. Aigner, N. Simonović, B. Solleder, J. Burgdörfer, and L. Wirtz *Phys. Rev. A* **82**, 062902 (2010).
 - [12] M. Sereno, S. Lupone, et al, to be submitted (2015).
 - [13] D. Danailov, K. Gärtner and A. Caro, *NIM B* **153**, p 191198 (1999).
 - [14] J. Seifert a, A. Schüller a, H. Winter K. Gärtner, *NIM B* **269**, 12121215, (2011).
 - [15] A. Zugarramurdi, M. Debiossac, P. Lunca-Popa, L. S. Alarcón, A. Momeni, H. Khemliche, P. Roncin, and A. G. Borisov *Phys. Rev. A* **88**, 012904 (2013).
 - [16] A. Zugarramurdi and A.G. Borisov, *Phys. Rev. A* **87**, 062902 (2013).
 - [17] M. Debiossac and P. Roncin *Phys. Rev. A* **90**, 054701 (2014).
 - [18] A. Schüller and H. Winter, *Phys. Rev. Lett.* **100**, 097602 (2008).
 - [19] J. Villette, A. G. Borisov, H. Khemliche, A. Momeni, and P. Roncin, *Phys. Rev. Lett.* **85** 3137 (2000)
 - [20] J. R. Manson, H. Khemliche, and P. Roncin, *Phys. Rev. B* **78**, 155408 (2008).
 - [21] P. Rousseau, H. Khemliche and P. Roncin, *NIM B* **258**, p13-17 (2007).
 - [22] P. Atkinson, M. Eddrief, V. H. Etgens, H. Khemliche, M. Debiossac, A. Momeni, M. Mulier, B. Lalmi, and P. Roncin, *Applied Physics Letters* **105**, 021602 (2014).
 - [23] T. Igel, R. Pfandzelter and H. Winter, *Europhysics Lett.* **35** 67 (1996)
 - [24] D. Borka, S. Petrović, N. Nešković, D. J. Mowbray, and Z. L. Mišković *Phys. Rev. A* **73**, 062902 (2006)